Mon. Not. R. Astron. Soc. **306,** 551–560 (1999)

Rapid variability in the synchrotron self-Compton model for blazars

Marco Chiaberge[1,3] and Gabriele Ghisellini[2]
[1]*Osservatorio Astronomico di Torino, Strada Osservatorio, 20, I-10025 Pino Torinese, Italy*
[2]*SISSA/ISAS International School for Advanced Studies, Via Beirut 2/4, I–34014 Trieste, Italy*
[3]*Osservatorio Astronomico di Brera, V. Bianchi, 46, I-22055 Merate, Italy*

Accepted 1999 February 8. Received 1999 February 8; in original form 1997 July 31

ABSTRACT

Blazars are characterized by large amplitude and rapid variability, indicating that the electron distribution is changing rapidly, often on time-scales shorter than the light-crossing time. The emitting region is sufficiently compact to let radiative losses dominate the cooling of high-energy electrons. We study the time-dependent behaviour of the electron distribution after episodic electron injection phases, and calculate the observed synchrotron and self-Compton radiation spectra. Since photons produced in different parts of the source have different travel times, the observed spectrum is produced by the electron distribution at different stages of evolution. Even a homogeneous source then resembles an inhomogeneous one. Time delays between the light curves of fluxes at different frequencies are possible, as illustrated for the specific case of the BL Lac object Mrk 421.

Key words: radiation mechanisms: non-thermal – methods: numerical – galaxies: active – BL Lacertae objects: individual: Mrk 421 – X-rays: galaxies.

1 INTRODUCTION

Variability is one of the defining properties of blazars, characterized by variations of their flux even of two orders of magnitude on time-scales of years, and smaller changes, but still up to factor of 2, on time-scales of hours/days. Observational efforts to characterize the variability behaviour, which started soon after the discovery of blazars, have been intensified in recent years, to study very fast fluctuations and possible correlation of fluxes at different frequencies (for a review see Ulrich, Maraschi & Urry 1997). This will hopefully shed light on the location of the emitting regions and on the nature of the acceleration mechanisms. Theoretical efforts, however, lag behind observations: the classical paper on time-dependent synchrotron and Compton flux is still Kardashev (1962), which solves the continuity equations for the particle distribution in cases where the cooling time $t_{\rm cool}$ can be considered longer than the light crossing time R/c for any energy. Atoyan & Aharonian (1997) and Mastichiadis & Kirk (1997) applied the results of solving the continuity equation for the electron distribution to the variations seen in the BL Lac object Mrk 421 and the Galactic superluminal source GRS 1915+105. In both cases, only the variability on time-scales longer than R/c were studied. On the other hand, significant variability often happens on time-scales extremely short in highly luminous (and compact) objects. This implies that the cooling time for the highest energy electron may well be shorter than R/c, even once the effect of Doppler boosting and blueshift is accounted for. This is also indicated by the behaviour of the light curves as seen, e.g., in the X-rays and in the optical, showing a quasi-symmetric behaviour, with rise and decay time-scales approximately equal (see, e.g., Massaro et al. 1996, Ghisellini et al. 1997, Urry et al. 1997 and Giommi et al. 1998), indicating that both times are connected to the light travel time across the source R/c, and therefore suggesting that the cooling times of the emitting electrons are shorter. This in turn implies that the electron distribution, at least at these energies, is significantly changing on time-scales shorter than R/c.

In these cases the knowledge of the time evolution of the particle distribution of the emitting electrons is not enough to construct theoretical light curves for the *observed* fluxes, since light travel time effects play a crucial role. The observer in fact sees, at any given time, photons produced in different part of the source, characterized by a particle distribution of a different age. The observed flux is then the sum of the emission produced by *different* particle distributions.

In Section 2 we present our method of solving the continuity equation for the emitting particle distribution, together with the assumptions made. In Section 3 we discuss illustrative examples of the time behaviour of the particle and photons distributions, taking care to elucidate the effects introduced by the different photon travel times. Besides considering simple illustrative cases where the injection of 'fresh' relativistic particles is assumed to occur simultaneously throughout the source, we also study more realistic cases which simulate the injection occurring when a shock front travels down a region of a jet. We summarize our results in Section 4. In Section 5 we apply our model to Mrk 421, to show how it is possible, even in our simplified model, to explain the time-lags observed in the hard and soft X-ray light curves. Finally, in Section 6 we discuss our findings.

2 THE MODEL

2.1 Assumptions

We assume that the emission is produced by a distribution of relativistic electrons injected in a region of typical dimension R embedded in a tangled magnetic field B, at a rate $Q(\gamma)$ [cm^{-3} s^{-1}] (γ is the Lorentz factor). Electrons lose energy by emitting synchrotron and synchrotron self-Compton radiation (SSC); they can also escape from the emitting region on a time-scale $t_{\rm esc}$, assumed to be independent of energy.

Our main purpose is to apply our calculations to the study of the short-time-scale variability of blazars, especially in frequency bands around and above the peaks of blazars spectral energy distribution. In these spectral regions synchrotron self-absorption is negligible, and consequently we neglect this heating effect in the kinetic equation (e.g. Ghisellini, Guilbert & Svensson 1988). Photon–photon collisions, producing electron–positron pairs, are also neglected, since we will deal with sources of small compactness $\ell \equiv L\sigma_{\rm T}/(Rmc^3)$ (Maraschi, Ghisellini & Celotti 1992).

The continuity equation governing the temporal evolution of the electrons distribution $N(\gamma, t)$ [cm^{-3}] is

$$\frac{\partial N(\gamma,t)}{\partial t} = \frac{\partial}{\partial \gamma}\left[\dot{\gamma}(\gamma,t)N(\gamma,t)\right] + Q(\gamma,t) - \frac{N(\gamma,t)}{t_{\rm esc}}, \tag{1}$$

where $\dot{\gamma} = \dot{\gamma}_S + \dot{\gamma}_C$ is the total cooling rate, given by

$$\dot{\gamma} = \frac{4}{3}\frac{\sigma_{\rm T} c}{m_{\rm e}c^2}[U_B + U_{\rm rad}(\gamma,t)]\gamma^2, \tag{2}$$

where $\sigma_{\rm T}$ is the Thomson cross-section, U_B is the magnetic field energy density, and $U_{\rm rad}(\gamma, t)$ is the energy density of the radiation field.

The cooling time-scale is assumed to correspond to synchrotron and self-Compton radiative losses:

$$t_{\rm cool} = \frac{3m_{\rm e}c^2}{4\sigma_{\rm T}c\gamma(U_B + U_{\rm rad})}. \tag{3}$$

This relation can be rewritten by assuming that all the radiation energy density is available for scattering, and that it corresponds to the compactness $\ell = 4\pi R\sigma_{\rm T}U_{\rm rad}/(m_{\rm e}c^2)$:

$$\frac{t_{\rm cool}}{R/c} = \frac{3\pi}{\gamma\ell(1 + U_B/U_{\rm rad})}. \tag{4}$$

Note that, for compactness values in the range 10^{-4}–10^{-1}, typical for the IR to γ-ray emission of blazars, the high-energy electrons cool faster than R/c.

2.2 Numerical method

We numerically solve equation (1), adopting the fully implicit difference scheme proposed by Chang & Cooper (1970), modified for our purposes, since we are dealing with a continuity equation with injection and escape terms, and no heating. The Chang & Cooper scheme allows us to find more stable, non-negative and particle number-conserving solutions. Moreover, that scheme significantly reduces the number of meshpoints required to obtain accurate solutions, and it is also appropriate for including heating terms (Ghisellini et al. 1988).

For all our runs we use an energy grid with equal logarithmic resolution: the energy meshpoints are defined as

$$\gamma_j = \gamma_{\rm min}\left(\frac{\gamma_{\rm max}}{\gamma_{\rm min}}\right)^{\frac{j-1}{j_{\rm max}-1}}, \tag{5}$$

where $j_{\rm max}$ is the meshpoints number, and the energy intervals are $\Delta\gamma_j = \gamma_{j+1/2} - \gamma_{j-1/2}$. Quantities with the subscript $j \pm 1/2$ are calculated at half-grid points. In the performed simulations a grid of 200 points has been used both for particle energy and photon frequency.

In order to discretize the continuity equation, we define

$$N_j^i = N(\gamma_j, i\Delta t), \tag{6}$$

$$F_{j\pm1/2}^{i+1} = \dot{\gamma}_{j\pm1/2}^{i} N_{j\pm1/2}^{i+1}, \tag{7}$$

and equation (1) can be written as

$$\frac{N_j^{i+1} - N_j^i}{\Delta t} = \frac{F_{j+1/2}^{i+1} - F_{j-1/2}^{i+1}}{\Delta\gamma} + Q_j^i - \frac{N_j^{i+1}}{t_{\rm esc}} \tag{8}$$

In this specific case we have $N_{j+1/2} \equiv N_{j+1}$ and $N_{j-1/2} \equiv N_j$, according to the prescriptions of Chang & Cooper (1970). We can now rewrite the continuity equation as

$$V3_j N_{j+1}^{i+1} + V2_j N_j^{i+1} + V1_j N_{j-1}^{i+1} = S_j^i, \tag{9}$$

where the V coefficients are

$$\begin{aligned} V1_j &= 0, \\ V2_j &= 1 + \frac{\Delta t}{t_{\rm esc}} + \frac{\Delta t\,\dot{\gamma}_{j-1/2}}{\Delta\gamma_j}, \\ V3_j &= -\frac{\Delta t\,\dot{\gamma}_{j+1/2}}{\Delta\gamma_j}, \end{aligned} \tag{10}$$

and

$$S_j^i = N_j^i + Q_j^i\,\Delta t\,. \tag{11}$$

The system of equations (9) forms a tridiagonal matrix, and it is solved numerically (e.g. Press et al. 1989). We tested our method with the analytic solutions given by Kardashev (1962) in the case of synchrotron radiation only and injection of a constant power law and monoenergetic distributions.

We then calculate the synchrotron emissivity $\epsilon_{\rm s}(\nu, t)$ [erg s^{-1} cm^{-3} sr^{-1} Hz^{-1}] of each distribution $N(\gamma_j, t_i)$ with

$$\epsilon_{\rm s}(\nu,t) = \frac{1}{4\pi}\int_{\gamma_{\rm min}}^{\gamma_{\rm max}} {\rm d}\gamma\, N(\gamma,t)\, P_{\rm s}(\nu,\gamma). \tag{12}$$

In the above formula $P_{\rm s}(\nu, \gamma)$ [erg s^{-1} Hz^{-1} sr^{-1}] is the single particle synchrotron emissivity averaged over an isotropic distribution of pitch angles

$$P_s(\nu,\gamma) = \frac{3\sqrt{3}}{\pi}\frac{\sigma_T c U_B}{\nu_B} t^2 \left\{ K_{4/3}(t)\,K_{1/3}(t) - \frac{3}{5}t\,[K_{4/3}^2(t) - K_{1/3}^2(t)] \right\} \tag{13}$$

(Crusius & Schlickeiser 1986; Ghisellini et al. 1988), where $t = \nu/(3\gamma^2\nu_B)$, $\nu_B = eB/(2\pi m_{\rm e}c)$, and $K_a(t)$ is the modified Bessel function of order a. We then calculate the synchrotron radiation field $I_{\rm s}(\nu, t)$ [erg s^{-1} cm^{-2} sr^{-1} Hz^{-1}] using the transfer equation

$$I_{\rm s}(\nu,t) = \frac{\epsilon_{\rm s}(\nu,t)}{k(\nu,t)}\left[1 - {\rm e}^{-k(\nu,t)R}\right]; \tag{14}$$

here $k(\nu, t)$ [cm^{-1}] is the absorption coefficient (e.g. Ghisellini & Svensson 1991)

$$k(\nu,t) = -\frac{1}{8\pi m_{\rm e}\nu^2}\int_{\gamma_{\rm min}}^{\gamma_{\rm max}} \frac{N(\gamma,t)}{\gamma p}\frac{\rm d}{{\rm d}\gamma}[\gamma p\, P(\gamma,\nu)], \tag{15}$$

where $p = (\gamma^2 - 1)^{1/2}$ is the particle momentum in units of $m_{\rm e}c$. In order to calculate the inverse Compton radiation field, we make the assumption that the synchrotron radiation instantaneously fills the whole of the emitting region (see also Section 2.3), and we take into

account the Klein–Nishina decline using the following approximation (Zdziarski 1986):

$$\sigma = \begin{cases} \sigma_T & \text{for } \gamma x < 3/4 \\ 0 & \text{for } \gamma x > 3/4, \end{cases} \tag{16}$$

where $x = h\nu/m_e c^2$. We approximate the energy density of the synchrotron radiation $U_{\rm rad,syn}(\gamma, t)$ by setting

$$U_{\rm rad,syn}(\gamma, t) = \frac{4\pi}{c} \int_{\nu_{\rm s,min}}^{\nu_{\rm max}(\gamma)} {\rm d}\nu \, I_s(\nu, t), \tag{17}$$

and the integration limits are defined as $\nu_{\rm min} = \nu_{\rm s,min}$ (minimum synchrotron emitted frequency) and $\nu_{\rm max}(\gamma) = \min[\nu_{s,max}, 3m_e c^2/(4h\gamma)]$.

The inverse Compton emissivity can be calculated, with the above assumptions, following Rybicki & Lightman (1979):

$$\epsilon_c(\nu_1) = \frac{\sigma_T}{4} \int_{\nu_0^{min}}^{\nu_0^{max}} \frac{{\rm d}\nu_0}{\nu_0} \int_{\gamma_1}^{\gamma_2} \frac{{\rm d}\gamma}{\gamma^2 \beta^2} N(\gamma) f(\nu_0, \nu_1) \, \frac{\nu_1}{\nu_0} \, I_s(\nu_0), \tag{18}$$

where ν_0 is the frequency of the incident photons, ν_1 is the frequency of the scattered photons, $\beta = v/c$, and the integration limits are

$$\gamma_1 = \max\left[\left(\frac{\nu_1}{4\nu_0} \right)^{\frac{1}{2}}, \gamma_{\rm min} \right], \tag{19}$$

$$\gamma_2 = \min\left[\gamma_{\rm max}, \frac{3}{4} \frac{m_e c^2}{h\nu_0} \right], \tag{20}$$

and where ν_0^{max} and ν_0^{min} are the extreme frequencies of the synchrotron spectrum. The function $f(\nu_0, \nu_1)$ is the spectrum produced by the single electron, scattering monochromatic photons of frequency ν_0 (see, e.g., Rybicki & Lightman 1979):

$$f(\nu_0, \nu_1) = \begin{cases} (1+\beta)\frac{\nu_1}{\nu_0} - (1-\beta); & \frac{1-\beta}{1+\beta} \le \frac{\nu_1}{\nu_0} \le 1 \\ (1+\beta) - \frac{\nu_1}{\nu_0}(1-\beta); & 1 \le \frac{\nu_1}{\nu_0} \le \frac{1+\beta}{1-\beta} \\ 0 & \text{otherwise.} \end{cases} \tag{21}$$

The inverse Compton radiation field is simply obtained as $I_c(\nu_1) = \epsilon_c(\nu_1) R$.

2.3 Slices

The knowledge of $N(\gamma, t)$ is not sufficient to reproduce properly the variability behaviour of blazars: observations in the optical band and at higher frequencies strongly suggest that the injection and/or the cooling times can be shorter than the light crossing time R/c. In this case the particle distribution evolves more rapidly than R/c, *and the observer will see a convolution of different spectra, each produced in a different part of the source*. Initially, the observer sees only the emission coming from fresh electrons located in the region ('slice') closest to her/him; then the inner parts of the source become visible, also showing 'young' spectra, while electrons in the front slices are evolving. After a time R/c all the emitting region will be visible: the back of it with fresh electrons, and the front of it with older electrons.

In order to reproduce this effect, we can divide the source of size R into n slices of equal thickness $R_{\rm sl}$, and then sum the contribution of each slice to obtain the correct observed spectrum. Note that the number of slices has to be chosen in order to have $R_{\rm sl}/c < t_{\rm min}$, where $t_{\rm min}$ is the shorter among the relevant time-scales (cooling, injection and escape time): in this way each slice can be considered as a *homogeneous* region, while the different slices are observed in a different evolution time, resembling an *inhomogeneous* emitting region.

We consider the case in which all slices have equal volumes, and assume a 'cubic' geometry, with the line of sight placed at 90° with respect to one face of the cube. This angle, besides corresponding to the simplest case, is transformed, in the laboratory frame, into a viewing angle of $\sim 1/\Gamma$, if the source moves with a Lorentz factor Γ, which is appropriate for blazars. Extension to different geometries (e.g., cylinder, sphere, etc.) is trivial, by properly weighting each slice volume. We will see that even in the simplest, 'cubic', case, time-lags among light curves at different frequencies are clearly observable.

We note that the light crossing time effects should be taken into account also for the correct calculation of the inverse Compton radiation: synchrotron photons in fact require a time R/c to fill the whole of the emitting region. This effect, relatively important for transient high-energy phenomena in Compton dominated sources, is however negligible for magnetic-dominated objects, and we neglect it in the present paper, due to the computing time it needs to be properly calculated. We plan to improve our numerical code in the future.

3 SIMULATIONS

3.1 Gaussian injection with $t_{\rm inj} \ll R/c$

We first examine the case of a narrow Gaussian electron distribution continuously injected for a time $t_{\rm inj} \ll R/c$ in a region of size $R = 10^{16}$ cm embedded in a tangled magnetic field $B = 1$ G. The injected distribution peaks at $\gamma = 10^5$. We measure the total injected power with the corresponding compactness, defined as $\ell_{\rm inj} \equiv L_{\rm inj}\sigma_T/(Rm_e c^3)$: in this case we use $\ell_{\rm inj} = 10^{-3}$. The injection stops at $t = R/(10\,c)$, and we set the escape time $t_{\rm esc} = 1.5R/c$. This is the value of $t_{\rm esc}$ used in all simulations, unless otherwise noted.

This case could represent a physical situation of a narrow region of the jet invested by a perturbation which activates the region. In this case R corresponds to the dimension perpendicular to the jet axis, while the width of the region could correspond to $\sim t_{\rm inj} c \ll R$. Besides possibly representing a real situation (even if highly idealized), this case is useful to show clearly the light crossing time effects. A more detailed discussion of the simulation of a region powered by a shock will be presented in Section 3.3.

In order to better understand the different behaviours of the evolution of the particle and photon distributions, we can roughly divide the electron distribution and the emitted synchrotron spectrum into three main energy ranges depending on the characteristic involved time-scales, with respect to R/c:

(i) low energy ($\gamma \lesssim 2 \times 10^2$, $\nu_{syn} \lesssim 10^{11}$ Hz), in which the cooling time is at least one order of magnitude longer than R/c, so particle escape is the leading effect;

(ii) medium energy ($2 \times 10^2 \lesssim \gamma \lesssim 2 \times 10^4$, $10^{11} \lesssim \nu_{syn} \lesssim 10^{15}$ Hz), in which the electron cooling time is comparable to R/c, so that the cooling time is comparable to the escape time, and

(iii) high energy ($\gamma \gtrsim 2 \times 10^4$, $\nu_{syn} \gtrsim 10^{15}$ Hz) in which $t_{\rm cool} \ll R/c$ (by at least one order of magnitude), so that the particle distribution evolves more rapidly than R/c.

In Fig. 1 we plot the electron distributions $N(\gamma)$ at different times, with high temporal resolution for the first instants, and lower temporal resolution for the rest of the evolution, when the cooling effects are much slower.

The higher energy part of the distribution reaches the equilibrium state in a very short time, and does not vary during the injection

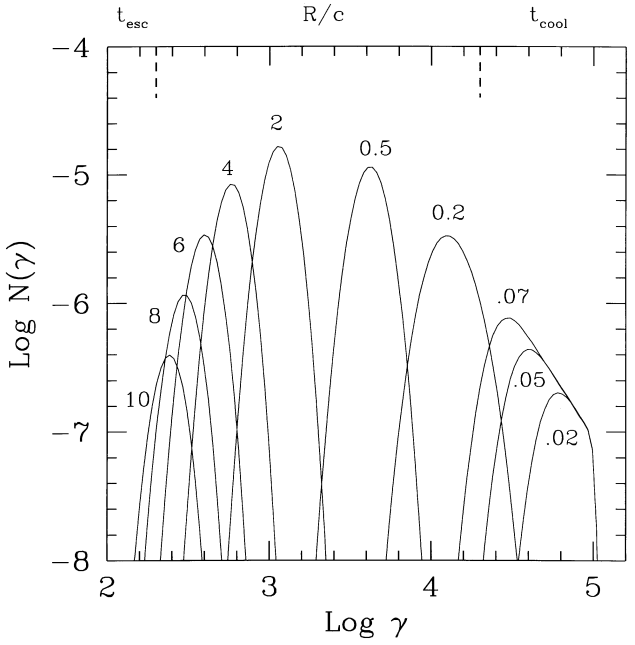

Figure 1. Evolution of the particle distribution $N(\gamma)$ corresponding to an injection of particles distributed in energy as a Gaussian, centred at $\gamma = 10^5$, for $t_{\rm inj} = 0.1R/c$. Labels indicate time after the beginning of the injection, in units of R/c (in the comoving frame). The escape time-scale is $t_{\rm esc} = 1.5R/c$. The energy range has been divided according to the relevant time-scales (top labels, see text).

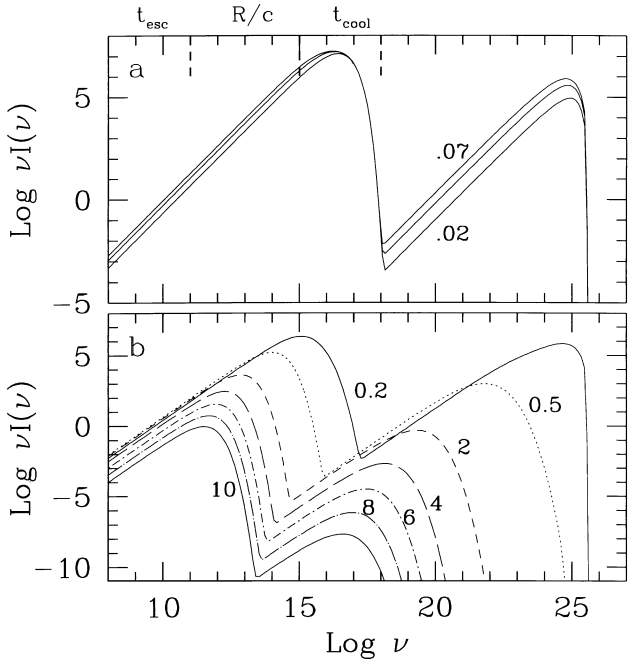

Figure 2. Evolution of the synchrotron self-Compton spectrum emitted by the particle distributions shown in Fig. 1, during (a) the injection phase, and (b) for $t > t_{\rm inj}$. Labels indicate the time after the beginning of the injection, in units of R/c (in the comoving frame). These spectra *do not* take into account light crossing time effects.

time, except for a small decay due to the increasing radiation field in the source, which increases the particle cooling. This is shown by the first three distributions in Fig. 1, labelled according to the time (in R/c units) after the beginning of the injection.

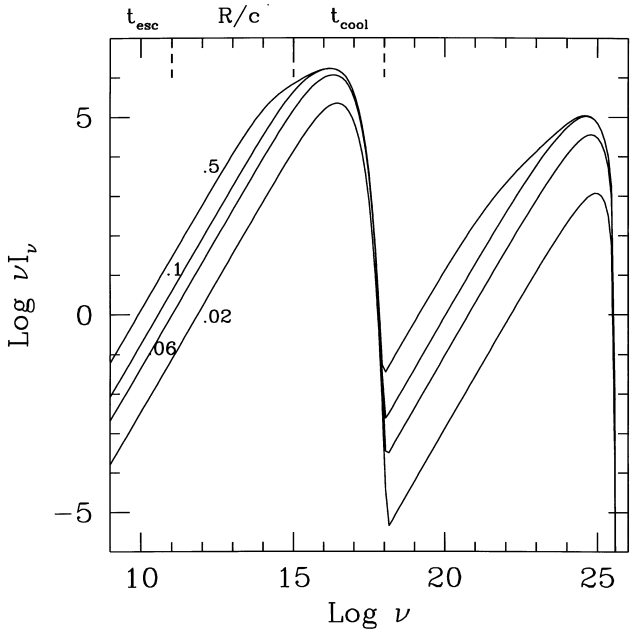

Figure 3. Evolution of the synchrotron self-Compton spectrum emitted by the particle distributions shown in Fig. 1, *taking into account* light crossing time effects. Note that the intensity is still rising at $t = 0.5\,R/c$ for frequencies under both the synchrotron and the Compton peaks, although the injection stops at $t = 0.1\,R/c$.

Fig. 2 shows the synchrotron self-Compton spectra produced by the distributions in Fig. 1, from $t = 0.02$ to $t = 10R/c$ *without considering light travel time effects*. The first instants (while the injection is active) are shown in Fig. 2(a), and the decay in Fig. 2(b). At frequencies above the synchrotron peak the cooling time is short, the equilibrium state is reached quickly and the flux is steady during the injection time, except for the very initial instants, not reproduced in Fig. 2(a). Note that since electrons are injected only at very high energies, their emission is first concentrated at high frequencies; only after some cooling time can they emit substantially at lower frequencies, simulating a new particle injection at lower energies. This can be seen in Fig. 2(b), where the flux at $\nu < 10^{13}$ Hz increases for $t > t_{\rm inj}$.

Fig. 3 shows the spectra produced by considering the effect of the *light crossing time*: as we already emphasized in Section 2.3, this effect must be included when the $N(\gamma)$ distribution evolves on time-scales shorter than R/c. In this case the observer will see different emissions coming from different regions of the source, *as the source itself were not homogeneous*. We stress that this is only due to the photon crossing time. In order to calculate properly the *observed* spectral evolution, we have to sum the correct contributions of the different source slices. The spectra shown in Fig. 3 correspond to the first instants of the evolution. Note that the intensity of synchrotron radiation is now increasing during the injection time also at frequencies above the peak. This is mainly due to the photon crossing time: when the electron cooling time is very short with respect to R/c (as it is, for example, for electrons emitting at the synchrotron peak at $\nu \sim 10^{17}$ Hz), the equilibrium state is reached quickly, and during the injection the observer receives photons coming from an increasing volume. After $t = t_{\rm inj}$, the flux remains steady until $t = R/c$, as can be easily seen also in the light curves (Section 3.1.1, Fig. 4). This effect is also shown by the Compton component.

Due to the rapid cooling, electrons at the highest energy reach

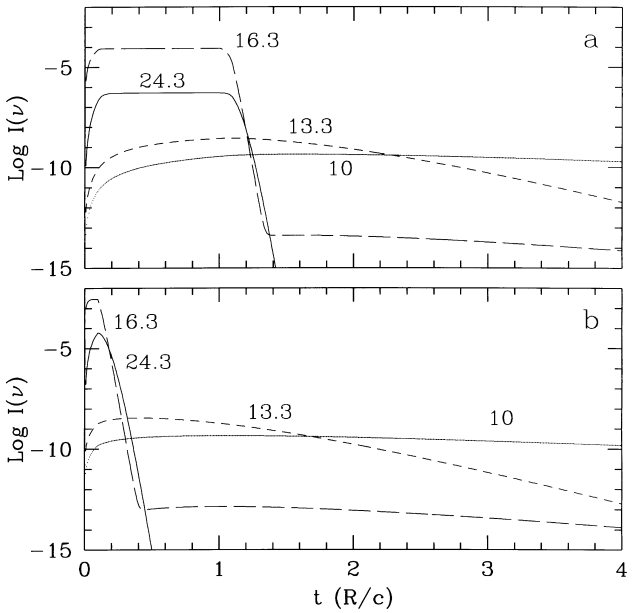

Figure 4. Light curves of the specific intensity at different frequencies, corresponding to the spectral evolution of Fig. 2, to illustrate light crossing time effects, included in (a) and ignored in (b). Labels correspond to the logarithm of the frequency, as seen in the comoving frame. For clarity, the intensity of each light curve has been multiplied by different constants.

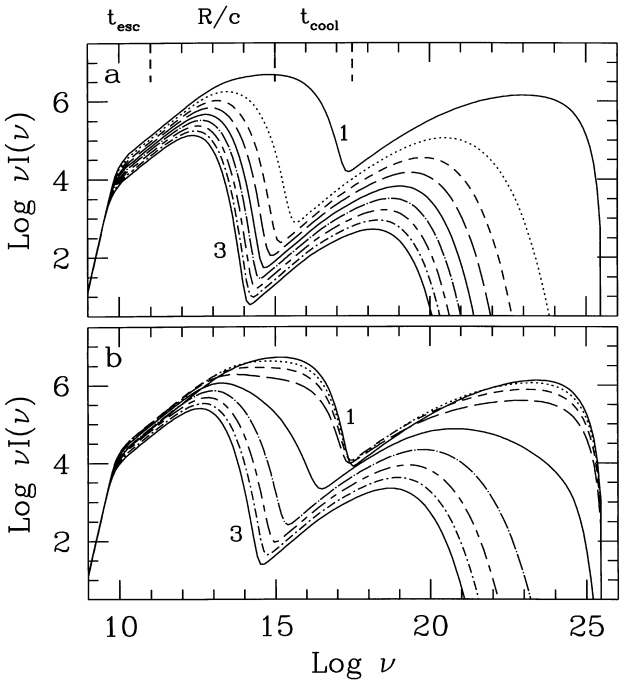

Figure 5. Evolution of the synchrotron self-Compton spectra calculated assuming to inject a power-law distribution, for $t_{\rm inj} = R/c$. In (a) light crossing time effects have been neglected, while in (b) they have been taken into account. For clarity, only the decaying phase is shown. The shown spectra are separated in time by $\Delta t = 0.25R/c$. Top labels divide the frequency range according to the relevant time-scales (see text).

equilibrium in a short time, and during the injection time the distribution at these energies remains steady. After $t_{\rm inj}$, it decays very rapidly. The corresponding synchrotron emission is then 'switched on' for a short time (during which it is constant), and then it is 'switched off'. At any given time (within R/c) the observer will then see a constant flux, produced by a single 'switched on' slice (which is 'running' across the source). This behaviour can be also seen in Fig. 4, where the light curves at different frequencies are shown.

3.1.1 Light curves

We can compare the light curves obtained considering or neglecting light crossing time effects. This is shown in Figs 4(a) and (b), respectively. We choose three frequencies on the synchrotron component, as they are characteristic of the three different energy ranges, and an additional frequency around the (initial) Compton peak.

Fig. 4(a) shows that at very low frequencies (i.e., $\nu \sim 10^{10}$ Hz), where $t_{\rm cool} \gg R/c$, the rise of intensity is slow, because it is controlled mainly by the the light crossing time R/c: the observer will see the first slice, then the first and the second slices, etc.; when the last slice become visible, the first one is still emitting, because particle cooling is very slow. Since electrons are injected mainly at high energies, they can emit substantially at lower frequencies only after some cooling time-scales: after $t = R/c$ the intensity is still rising in some slices, causing the flux at these low frequencies to peak at $t > R/c$.

The intensity at higher frequencies peaks instead at earlier times. At very high synchrotron frequencies ($\nu \sim 10^{16}$ Hz and above) we will have a plateau, because both $t_{\rm cool}$ and $t_{\rm inj}$ are much shorter than R/c: the electrons cool so fast that we will see a single slice 'running' across the source, as mentioned above.

The shape of the decay phase is different for different frequencies: it is controlled mainly by $t_{\rm esc}$ at very low frequencies (see the light curve at $\nu = 10^{10}$ Hz), while cooling dominates at higher frequencies.

Note that the decay in the low-frequency light curves in Fig. 4(a) are very similar to those in Fig. 4(b), while the entire high-frequency light curves and the initial instants of the low-frequency ones cannot be reproduced without including the light crossing time effect. This happens because in these last two cases R/c is longer than $t_{\rm cool}$ or the injection time respectively.

In Fig. 4 we also show the $\nu = 2 \times 10^{24}$ Hz light curve, which is close to the (initial) peak of the Compton emission component. The shape of this curve is very similar to that of the $\nu = 2 \times 10^{16}$ Hz one, which is close to the synchrotron peak, because emission comes mainly from electrons of approximately the same energy.

3.2 Power-law injection with $t_{\rm inj} = R/c$

We now show the case of electrons distributed in energy as a power law $Q(\gamma) \propto \gamma^{-p}$ ($p > 0$), continuously injected for $t_{\rm inj} \sim R/c$. Input parameters for this case are: $R = 10^{16}$ cm, $Q(\gamma) \propto \gamma^{-1.7}$ cm^{-3} s^{-1} with $\gamma_{\rm min} = 1$, $\gamma_{\rm max} = 10^5$, $\ell_{\rm inj} = 10^{-3}$, $B = 1$ G, $t_{\rm esc} = 1.5R/c$.

We plot the time-dependent spectra from $t = R/c$ to $t = 3R/c$ in Fig. 5(a) without considering the effect of the slices, and in Fig. 5(b) we summed the correct contribution of the different slices.

Also, in this case we roughly divide the synchrotron component into three energy ranges:

(i) for $\nu < 10^{11}$ Hz the corresponding electron cooling time is much longer than R/c, and the decay of the flux (for $t > t_{\rm inj}$) is mainly due to particle escape;

(ii) for $\nu > 10^{15}$ Hz we have $t_{\rm cool} \ll R/c$: this is the part of the emitted spectrum in which we can see the greatest differences between the behaviours reported in Figs 5(a) and (b); in other

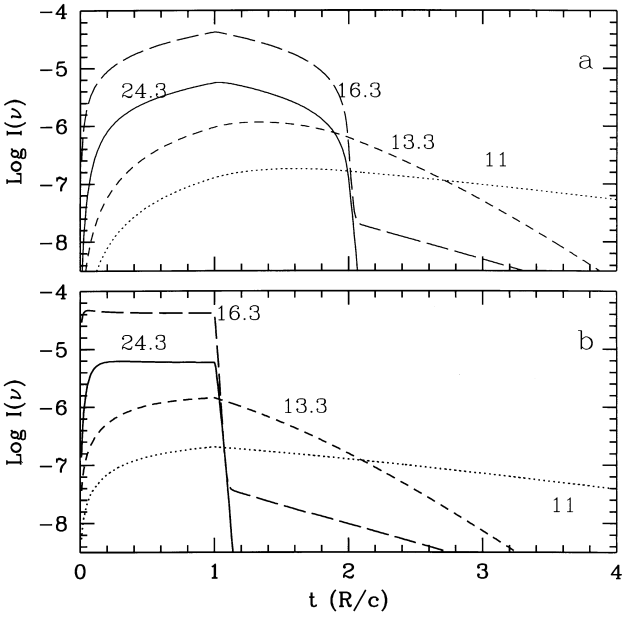

Figure 6. Light curves of the specific intensity at different frequencies, corresponding to the spectral evolution of Fig. 5, to illustrate light crossing time effects, included in (a) and ignored in (b). Labels correspond to the logarithm of the frequency, as seen in the comoving frame. For clarity, the intensity of each light curve has been multiplied by different constants.

words, in this range of frequencies it is strictly necessary to take into account the different photon crossing times in order to correctly reproduce the evolution of the emitted spectrum, and

(iii) in the middle region we have $t_{\rm cool} \sim R/c$.

It is interesting to compare the flux behaviour, after the stop of the injection, in the spectral region in which $t_{\rm cool} \ll R/c$: in Fig. 5(a) (light crossing time effects ignored) we see that at the highest synchrotron frequencies the decay is very rapid, since the entire source closely follows the decay of the corresponding electron distribution.

In the second case (Fig. 5(b), taking into account light crossing time effects) the behaviour is more complex, and after the end of the injection the emission falls showing three different phases:

(1) $t \gtrsim R/c$: we have a slow decay; we receive the emission from the distribution that starts to cool from the front slices, while the back slices are still 'switched on'.

(2) $t \sim 2R/c$: when almost the entire source is (seen) cooled, the decay speeds up, because the only important contributions are given by the back slices,

(3) $t \sim 3R/c$: the entire source will not contain highly energetic electrons any longer, and the emission at $\nu > 10^{15}$ Hz is dominated by the Compton component, produced by electrons of relatively small energy, whose cooling time is long. Correspondingly, at these frequencies the decay has a long and slow tail (see the curves for $\log \nu = 16.3$ in Figs 6 and 8).

This behaviour is illustrated by the light curves shown in Fig. 6.

For the flux at the highest (Compton) frequencies, the behaviour is similar to the synchrotron flux, up to $t \sim 2R/c$, after which the flux disappears.

It is important to note that just after the end of the injection, when high-energy electrons are present and synchrotron photons are scattered at $\nu \geq 10^{24}$ Hz, we find similar variability factors for frequencies above the two peaks, contrary to the 'normal' behaviour which is characterized by a quadratic dependence of the Compton flux with respect to the synchrotron flux. This is due to the fact that the Compton scattering at these frequencies is in the Klein–Nishina regime: high-energy electrons efficiently scatter seed photons of frequencies $h\nu/m_{\rm e}c^2 < 1/\gamma$ (see equation 16). For the highest energy electrons the available synchrotron photons for scattering are less, reducing the variability amplitude (see, e.g., Ghisellini, Maraschi & Dondi 1996).

3.2.1 *Light curves*

We report in Figs 6(a) and (b) the light curves at four different frequencies, considering or not light crossing time effects. We can see that taking them into account we can have symmetric light curves, with equal rising and decaying phases, at frequencies for which $t_{\rm cool} \ll R/c$. The cooling time of the electrons emitting at high frequencies (10^{15}–10^{17} Hz) is much shorter than R/c, and the electron distribution remains steady for the entire injection time. This implies that for $t < R/c$ the observer sees an increase of the flux due to the increasing 'switched on' volume of the source. After $t = R/c$, the front slices 'switch off', and the total flux decreases. This corresponds to symmetric light curves without plateaux. At lower frequencies, at which $t_{\rm cool} > R/c$, the decay is slower than the rise, and the light curves are asymmetric.

Another remarkable effect is the existence of time-lags among the light curves at different frequencies: it is easy to see that the emission peaks are not reached at the same time and the flux at the highest frequencies appears to lead. This behaviour can be contrasted with that shown in Fig. 6(b), i.e., neglecting light crossing time effects: in this case we see the formation of a plateau at high frequencies, where the equilibrium state is reached first.

To explain the time-lags in Fig. 6(a) consider the time $t = t_{\rm inj} = R/c$: the observer sees the stop of the particle injection in the 'front' of the source, while the back of the source is still 'switched off'. In other words, at this time the observer is receiving the spectra emitted by a population of electrons at $t_{evol} = R/c$ (from the front of the source) and at $t_{evol} = 0$ (from the back of the source). At later times in the front of the source the electron distribution starts to decay (with a corresponding decay of the emitted flux), while in the back the flux is still rising until the particle distribution reaches, after some $t_{\rm cool}$, the equilibrium state. This combination of slices in which the emitted flux is increasing and slices in which the decaying phase has already started, determines the position of the peak on each light curve. Note that if the electron cooling time is very short (for example, in the case of the $\nu = 10^{16}$ Hz in Fig. 6), the equilibrium state is reached in a very short time with respect to R/c: after the injection stops, each slice is quickly *turned off*, and the peak of the light curve is reached soon after $t = t_{\rm inj} = R/c$. In light curves corresponding to lower energy electrons the peak will occur later, because the equilibrium state is reached later: after the stop of the injection the flux is slowly decreasing in the front of the source, while it is still increasing in the back. The longer the particle cooling time, the longer the time that the light curve needs to reach the maximum.

We emphasize that the different cooling times of the electrons responsible for the emission at different frequencies introduce more visible time-lags if the light crossing time effects are included, as can be seen comparing the light curves for the high synchrotron frequencies shown in Figs 6(a) and (b).

3.3 Simulation of a shock

We assume that a shock of longitudinal dimension R and width

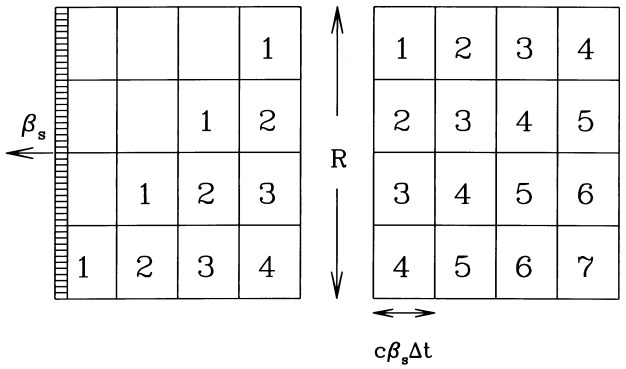

Figure 7. Schematic illustration of the composition of spectra arriving at the observer at the same time, but leaving each shell at a different time, hence produced by electrons of a different age. The observer is assumed to be located at 90° to the shock velocity (bottom of the figure) in the frame comoving with the particle flow. In the left-hand panel the shock has been active for a time $R/\beta'_s c$ since the beginning of the injection. The number in each cell indicates the 'age' of the electrons. Note that above the 'diagonal' line (cells without number), photons had not enough time to reach the observer. The right-hand panel shows how to sum the contributions of the cells at the time equal to $2R/\beta'_s c$, in the case that the shocks stops to inject particles after $t_s = R/c$. At later times each cell will contribute to the emission with an older distribution, and correspondingly the number characterizing each shell will increase by one unit at each time-step Δt.

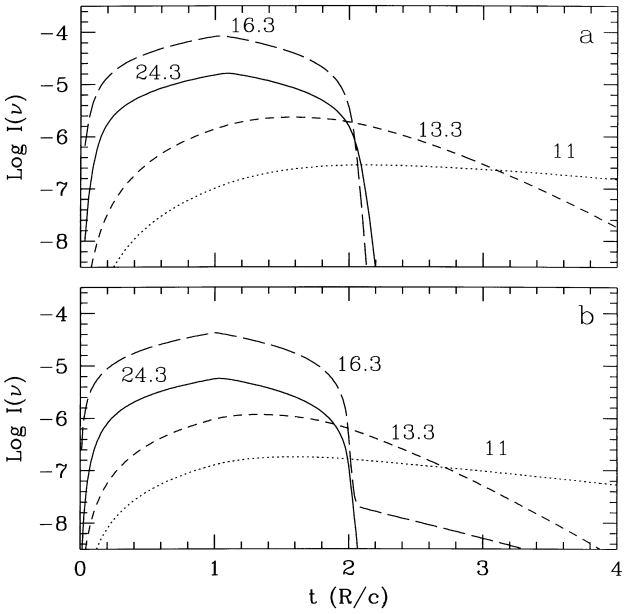

Figure 8. (a) Light curves at different frequencies (as seen in the comoving frame) corresponding to a simulation of a shock of width $r = t_{\rm inj}\beta'_s c$, $t_{\rm inj} = 0.1R/c$, injecting energetic particles for a time $t_s = R/c$. All other parameters are the same as in the simulations shown in Fig. 6. In panel (b) we report the the light curves already shown in Fig. 6(a) in the case $t_{\rm inj} = R/c$. For clarity, the intensity of each light curve has been multiplied by different constants.

$r \ll R$ runs along a region of the jet of same dimension R (perpendicular to the jet axis). Particle flows along the jet with a velocity βc. In the frame comoving with this flow the shock moves with a velocity $\beta'_s c$. As in the previous sections, we assume that the observer is located at an angle $1/\Gamma = \sqrt{1-\beta^2}$ from the jet axis, such that the viewing angle in the comoving frame is 90°. We assume that the shock is active for a time t_s, as measured in the comoving frame. At a given location, the shock accelerates particles for a time $t_{\rm inj} = r/(\beta'_s c)$.

To show how to sum correctly the different contributions of different emitting regions, we sketch in Fig. 7 an illustrative example with a small number of different regions. In this case, each slice parallel to the jet axis is characterized by different electron distributions: 'young' electrons close to the shock front, and older ones far from it. It is therefore necessary to subdivide each slice into an appropriate number of 'cells' (see Fig. 7). The velocity of the shock in the frame comoving with the particle flow determines the size of the cells in the direction parallel to the jet axis, and then the total emitting volume.

Fig. 8(a) shows the light curves obtained in the case of a shock of width $r = t_{\rm inj}\beta'_s c$, with $t_{\rm inj} = 0.1R/c$ active for a time $t_s = R/c$, with all other parameters equal to the case of Section 3.2.

Comparing Figs 8(a) and (b), one can see that in the shock case we obtain further delays between different frequencies, due to the different way of summing the spectra produced at different time-steps.

From these simulations we can conclude that there are no qualitative differencies between the light curves in the 'homogeneous' case with $t_{\rm inj} = R/c$, except for the occurrence of further time delays between light curves at different frequencies.

3.4 Multiple rapid injections

In Fig. 9(a) we show the light curves resulting from discontinuously injecting a Gaussian distribution of particles, centred at $\gamma = 10^5$. In the shown case, we have assumed that there are 17 injection phases, lasting from $t_{\rm inj} = 0.1R/c$ to $t_{\rm inj} = R/c$, separated by different times, and that $t_{\rm esc} = 8R/c$. The electron injection rates are equal for all cases.

It can be seen that these injection phases can be resolved at the highest synchrotron frequencies, while they merge at lower frequencies, where the memory of the different injection phases is lost. At energies at which $t_{\rm cool} > R/c$, the electron distribution builds up, since electrons cool on a time-scale longer than the time separation between different injection phases. This introduces both a smoothing of the corresponding light curve and a time delay with respect to higher frequency light curves.

The series of short injection phases separated by short times makes the synchrotron flux at the highest frequencies to flicker. The superposition of the different distributions corresponding to each injection phase prevents the formation of the 'plateau', characteristic of a single short time injection. This also causes the variability time-scales to be shorter than R/c.

In Fig. 9(b) we show the time evolution of three spectral indices ($\alpha_{11.5-12.5}$, $\alpha_{12.5-14.5}$ and $\alpha_{14.5-16.5}$, connecting the flux at $\log\nu = 11.5$ and 12.5, the flux at $\log\nu = 12.5$ and 14.5, and the flux at $\log\nu = 14.5$ and 16.5, respectively, where frequencies are measured in Hz). The spectral indices can vary (even by a large amount) during the major injection phases, while they remain within a narrow range during the flickering phases.

4 DISCUSSION

We summarize here the main characteristic of the light curves for different values of $t_{\rm inj}$, $t_{\rm cool}$ and $t_{\rm esc}$:

(i) $t_{\rm inj} \ll R/c$
  – when $t_{\rm cool} \gg R/c$ we see a slow rise of intensity, mainly controlled by the light crossing time R/c: the maximum of

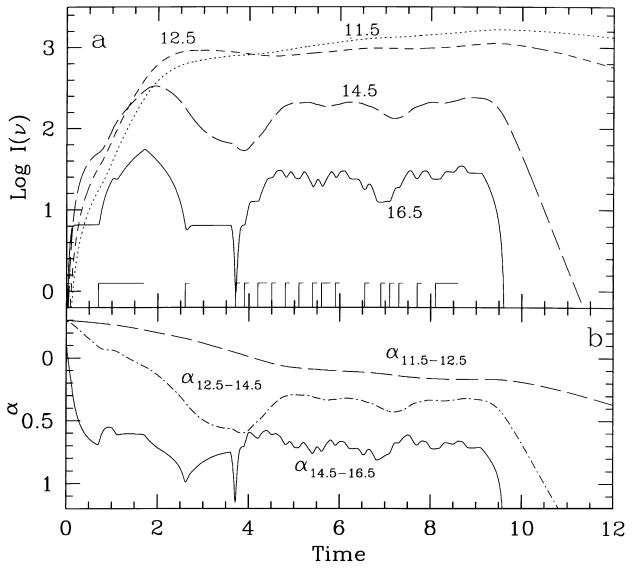

Figure 9. Light curves of the specific intensity at different frequencies (as seen in the comoving frame) and spectral indices resulting from multiple injection phases. For clarity, the intensity of each light curve has been multiplied by different constants. Time is in units of R/c. The 'L'-shaped ticks at the bottom of panel (a) indicate the duration of the injection events.

intensity is reached for $t > R/c$, and depends on $t_{\rm cool}$ and $t_{\rm esc}$. At low frequencies, where $t_{\rm cool} \gg t_{\rm esc}$, the decay of the emission is controlled by $t_{\rm esc}$, while at frequencies where $t_{\rm cool} \leq t_{\rm esc}$ the leading effect is cooling;
– when $t_{\rm cool} \simeq R/c$ the rising shape of the light curve is similar to the above case. The maximum of intensity is now reached at $t \sim R/c$, and the shape of the decay is controlled by $t_{\rm cool}$; in the special case in which $R/c \sim$ a few times $t_{\rm cool}$ we have a symmetric light curve;
– if $t_{\rm cool} \sim t_{\rm inj}$ we have a fast rise of intensity ($t_{rise} \simeq t_{\rm inj}$) and then a plateau (or a very slow rise in the shock case) until $t \sim R/c$. For $t > R/c$ the decay is as fast as the initial rise.

(2) $t_{\rm inj} \sim R/c$
– if $t_{\rm cool} \gg R/c$ we see a slow rise, the maximum is at $t \approx 1.5R/c$, and the decay is due to escape if $t_{\rm cool} \gg t_{\rm esc}$;
– if $t_{\rm cool} \sim t_{\rm inj} \sim R/c$ the shapes of the rising and decaying phases are very similar, resulting in a symmetric light curve;
– where $t_{\rm cool} \ll R/c$ both the rise and the decay are controlled by the light crossing time, and we have symmetric light curves with time-lags depending on the different cooling times;

(3) if $t_{\rm inj}$ is much longer than R/c and $t_{\rm cool}$ the light curve will have a plateau, because the long injection time allows the entire source to reach equilibrium.

The main difference between injecting electrons at high energies ('monoenergetic' or Gaussian injection) and injecting a power-law (with $p > 0$) distribution is that in the first case the emission will be concentrated first at high frequencies, and only after some $t_{\rm cool}$ can electrons emit substantially at lower frequencies. This simulates a sort of a 'new' injection at low energies, that continues for $t > t_{\rm inj}$, and produces a time delay between the peak of the emission at different frequencies.

If the emitting plasma has bulk motion, we must take into account the effects of beaming. If Γ is the bulk Lorentz factor, θ the viewing angle, and $\delta = [\Gamma(1 - \beta\cos\theta)]^{-1}$ the beaming factor, the observed intensity is $I(\nu) = \delta^3 I'(\nu')$ and $t = t'/\delta$, where $I'(\nu')$ and t' are the comoving intensity and comoving time-scales, respectively.

Observations of variability in BL Lac objects suggest the simultaneous presence of different variability time-scales on each source (e.g. Massaro et al. 1996; Ghisellini et al. 1997), suggesting that the variations can originate in more than one component: a larger one can take into account of the longer time-scale variations, and smaller ones can originate in the rapid flares. Flares are observed at almost all wavelengths (depending on each source characteristics), and can have different durations (from hours to days). The occurrence of outbursts with symmetric shape (similar rise and fall) has been recently reported for well-monitored sources, especially in the optical band (Massaro et al. 1996; Ghisellini et al. 1997) and in the X-ray band (Urry et al. 1997). According to our results, this behaviour can originate only in two cases:

(i) $t_{\rm inj} \ll R/c \sim t_{\rm cool}$, and
(ii) $t_{\rm inj} \sim R/c$ and $t_{\rm cool} \ll R/c$.

In case (i) symmetric light curves are present only within a very small range of frequencies ($t_{\rm cool} \sim R/c$), while in case (ii) quasi-symmetric light curves can occur at all frequencies corresponding to particle cooling time-scales shorter than R/c. Furthermore, the second case can be interpreted as a result of a shock lasting for a time $t_{\rm inj} \sim R/c$.

Note that the underlying component has not been included in the previous simulations (Sections 3.1 and 3.2), which describe only the evolution of the 'flaring' component. To reproduce the variability behaviour of blazars correctly, it is therefore necessary to take into account the presence of a quasi-stationary component, *diluting* the variability of the flaring component.

Finally, note that the simulations in Section 3.4 of a shock active for a time R/c are similar to the corresponding 'homogeneous' case, with slightly longer time delays between light curves at different frequencies.

5 APPLICATION TO MRK 421

Mrk 421 is one of the nearest BL Lac Lac objects ($z = 0.03$), and it is classified as XBL (X-ray-selected BL Lac) (Giommi et al. 1990; Hewitt & Burbidge 1993). In the overall spectral energy distribution $[\nu - \nu F(\nu)]$ the X-ray emission smoothly connects to the optical and UV. It is generally believed that this component is due to synchrotron emission. Mrk 421 is a faint *EGRET* source with a flat GeV spectral index (Sreekumar et al. 1996), and it was the first blazar to be detected at TeV energies (Punch et al. 1992). In the optical, UV, X-ray and TeV bands it shows strong and rapid flux variability (Buckley et al. 1996).

In 1994 May the *ASCA* satellite revealed an X-ray flare (Takahashi et al. 1996) during an high state of TeV emission (Macomb et al. 1995). Observations report an increase of a factor ~2 of the 2–10 keV flux, with a doubling time-scale of ~12 h, while much lower amplitude variability is present in the IR, optical, UV and GeV (*EGRET*) bands. Takahashi et al. (1996) found a time-lag between hard X-rays (2–7.5 keV) and soft X-rays (0.5–1 keV) of ~1 h: the hard X-rays lead the soft X-rays. They interpret this as due to synchrotron cooling. With the numerical code described in the previous sections we can qualitatively reproduce this behaviour, first by fitting the high and the low states (Macomb et al. 1995) as equilibrium SSC spectra, and then by generating simulated light curves at all frequencies. In Fig. 10 we report the simultaneous spectra taken during the high and low states (data from Macomb et al. 1995, 1996, using $H_0 = 50\,{\rm km\,s^{-1}\,Mpc^{-1}}$, $q_0 = 0.5$). The parameters used for the fits are reported in the figure caption.

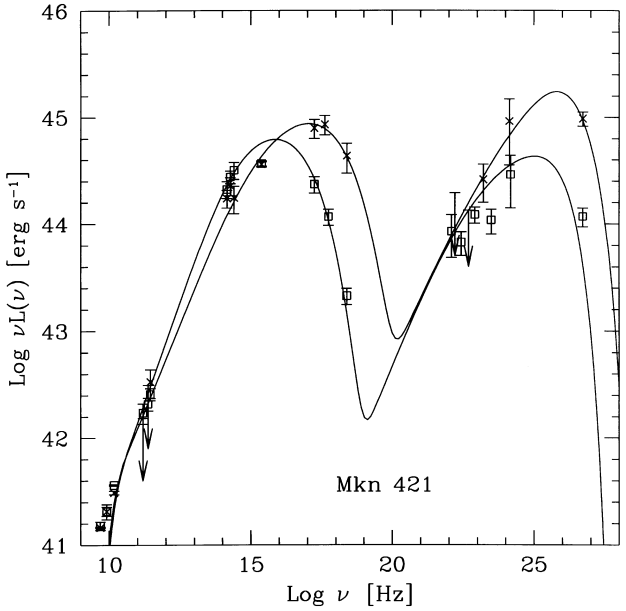

Figure 10. High and low states of Mrk 421 during the 1994 multiwavelength campaign (Macomb et al. 1995); continuous lines are equilibrium SSC models. We found satisfactory fits with the following parameters: $R = 4.8 \times 10^{16}$ cm, $B = 0.08$ G, injection law $Q(\gamma) \propto \gamma^{-1.5} \exp(-\gamma/\gamma_{\max})$ with $\gamma_{\min} = 1$, $\gamma_{\max} = 1.3 \times 10^5$, $t_{\rm esc} = 4R/c$, injected compactness $\ell_{\rm inj} = 9 \times 10^{-5}$, beaming factor $\delta = 15.5$ *(low state)*; $R = 4.8 \times 10^{16}$ cm, $B = 0.04$ G, $Q(\gamma) \propto \gamma^{-1.7} \exp(-\gamma/\gamma_{\max})$ with $\gamma_{\min} = 1$, $\gamma_{\max} = 8.5 \times 10^5$, $\ell_{\rm inj} = 2.5 \times 10^{-4}$, $t_{\rm esc} = 3R/c$, $\delta = 15.5$ *(high state)*.

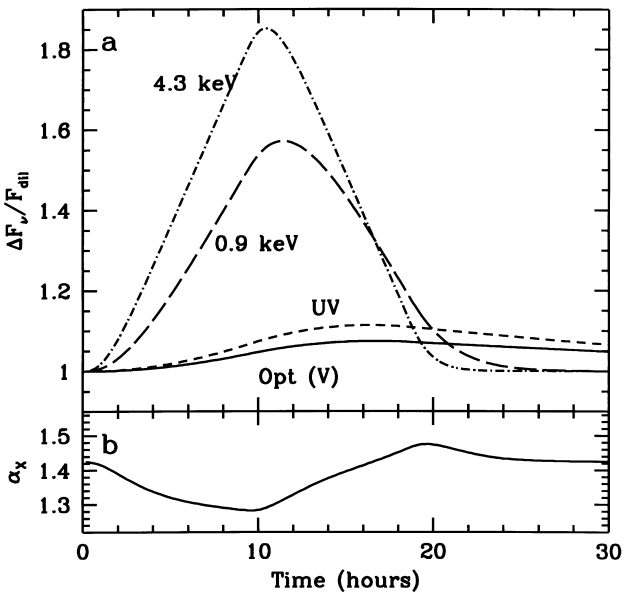

Figure 11. Light curves at different energies, reproducing the rapid flare shown by Mrk 421 on 1994 May 16. In (a) we plot the flux at different frequencies normalized to the steady component; in (b) the spectral index connecting the 4.3- and 0.9-keV fluxes is shown. Times and frequencies take into account of the beaming factor δ.

We assumed that the rapid variability revealed by *ASCA* during the highly active X-ray/TeV state is due to the sum of a rapidly evolving component and a quasi-constant one, corresponding to the high-state fit. We add to this constant emission a variable component, for which we found the following parameters: $R = 1.5 \times 10^{16}$ cm, $B = 0.13$ G, $\delta = 15.5$, $\ell_{\rm inj} = 1.5 \times 10^{-3}$, $Q(\gamma) \propto \gamma^{1.4} \exp(-\gamma/\gamma_{\max})$ between $\gamma_{\min} = 10^3$ and $\gamma_{\max} = 8.5 \times 10^5$. We perform the simulation in the shock case with the following parameters: $r_{\rm s} = 0.1R/c$, $t_s = R/c$ and $\beta'_{\rm s} \sim 1$.

We plot the obtained light curves at four different frequencies in Fig. 11. Note that the flux is still increasing at all reported frequencies for $t > t_s(1+z)/\delta$, which corresponds to $t \sim 9$ h: this is due to the different evolving state of the electrons in the different cells.

Because of the photon travel time, when the injection stops (at $t_{\rm s} = R/c$) the observer still sees the emission from the back of the source produced by the *increasing* particle distribution. Therefore the maximum flux is observed at a time greater than R/c, by an amount depending on the cooling time: the flux at the highest frequencies peaks first, followed by the flux at lower frequencies. As a consequence, the flux at the synchrotron peak (X-ray band) leads the flux at lower frequencies, and time-lags can be observed even between close frequencies within the same band.

Another consequence of our modelling is the prediction of time-lags between the synchrotron and the self-Compton fluxes. While the X-ray and the TeV emission are probably produced by the same electrons, the most effective seed photons for the TeV emissions are in the (observed) optical–UV band, due to the Klein–Nishina decline of the scattering cross-section. In the case discussed here, the electron population producing the optical–UV emission builds up, as a consequence of particle cooling, some time after the beginning of the injection. Optical–UV and TeV emissions should therefore be nearly simultaneous, lagging the X-ray emission. A delay between X-ray and TeV emissions can also be introduced by taking into account the different light travel times of the seed photons to be scattered at high energies, as mentioned in Section 2.3, but to be more quantitative we must await a more detailed numerical treatment.

A time-lag between X-ray and TeV fluxes should exist only if the seed photons for the scattering are produced locally. In the alternative case of seed photons coming from external regions (by, e.g., a dusty IR torus), we expect to observe a simultaneous rise in the X-ray and TeV fluxes of the same factor. Note that the 'external' radiation could also come from adjacent regions of the flaring component, i.e. the ones responsible for the 'diluting' component. Also, in this case the X-ray and the TeV fluxes, being produced by the same electrons, should vary linearly and simultaneously.

6 CONCLUSIONS

By summing the contribution of different slices of the source, the observer receives photons produced by particle distributions of different ages, a situation which resembles the one occurring in an inhomogeneous source. This effect is important whenever the particle distribution evolves on time-scales shorter than R/c. Despite the fact that this effect tends to smooth out rapid variations, time delays between light curves at different frequencies are observable, as illustrated for the hard/soft X-ray emission of Mrk 421. Our results are particularly important for the observed rapid variability of blazars, where the variability time-scales indicate extremely compact emission regions, thus large magnetic and radiation energy densities, and consequently cooling time-scales shorter than the light crossing time R/c. This is also a necessary condition for having symmetrical flares (equal rising and decay time-scales), often observed in the optical and in the X-ray band. Note that the case of 3C 279, one of the best studied blazars which showed asymmetric light curves at high energies, is probably

different, because the high-energy emission can be inverse Compton scattering off seed photons produced externally to the jet, and the resulting light curve can be connected to the geometrical distribution of these seed photons: for example, if an active blob passes through the broad-line region (BLR), there will be enhanced inverse Compton emission as long as the blob is inside the BLR, and a sudden drop when the blob moves outside the BLR.

Within the synchrotron self-Compton scenario, the symmetrical behaviour of the light curves near or above the peak of the synchrotron emission can be contrasted with the light curves at lower frequencies, characterized by cooling (and escape) time-scales longer than R/c. In this case the light curves should be asymmetric, with a rising phase lasting $\gtrsim R/c$ (if $t_{\rm inj} \sim R/c$), and a decaying phase lasting for $t_{\rm cool}$ (or $t_{\rm esc}$, if shorter than $t_{\rm cool}$). Sources with different magnetic field and/or different compactnesses should behave differently, since for very compact (or larger magnetic field) sources, the cooling time can be shorter than R/c for a wider range of electron energies, resulting in symmetric light curves for a wider range of frequencies.

We stress that symmetric light curves without plateaux strongly constrain the injection and the cooling time-scales: if both these times are much longer than the light crossing time R/c, the light curve is not symmetric; if both time-scales are much shorter than R/c, the curve is symmetric, but a plateau forms, while if the injection time is shorter than R/c and the cooling time is of the same order, a symmetric light curve is possible (without plateau), but only at one specific frequency. Therefore symmetric light curves without plateau at more than one frequency are possible only if the injection lasts for R/c and the cooling time is shorter than R/c.

A more complex behaviour is possible if the injection of relativistic electrons is impulsive and repeated several times within one light crossing time R/c. In this case the synchrotron flux at the largest frequencies responds to the different injection phases, and the repeated injections can make the plateaux in their light curve to disappear. Variations of relatively small amplitude are possible in very short times, which would lead us to calculate variability time-scales shorter than R/c. At lower frequencies, where cooling times are longer, the electron distributions corresponding to different injections can build up and the memory of the individual injection phases is lost. At these frequencies the light curves are smoother, and they can have apparent delays (with respect to higher frequency light curves) produced by this 'build-up' effect.

ACKNOWLEDGMENTS

We thank G. De Francesco for help during the preparation of the numerical code, and G. Bodo, A. Celotti and L. Maraschi for useful discussions.

REFERENCES

Atoyan A. M., Aharonian F. A., 1997, in Ostrowski M., Sikora M., Madejski G. M., Begelman M. C., eds, Relativistic Jets in AGNs. Krakow, Poland, p. 324
Buckley J. H. et al., 1996, ApJ, 472, L9
Chang J. S., Cooper G., 1970, J. Computational Physics, 6, 1
Crusius A., Schlickeiser R., 1986, A&A, 164, L16
Ghisellini G., Svensson R., 1991, MNRAS, 252, 313
Ghisellini G., Maraschi L., Dondi L., 1996, A&AS, 120, 503
Ghisellini G. et al., 1997, A&A, 327, 61
Ghisellini G., Guilbert P., Svensson R., 1988, ApJ, 334, L5
Giommi P. et al., 1990, ApJ, 356, 432
Giommi P. et al., 1998, A&A, 335, L5
Hewitt A., Burbidge G., 1993, ApJS, 87, 451
Kardashev N. S., 1962, SvA, 6, 317
Macomb D. J. et al., 1995, ApJ, 449, L99
Macomb D. J. et al., 1996, ApJ, 459, L111 (Erratum)
Maraschi L., Ghisellini G., Celotti A., 1992, ApJ, 397, L5
Massaro E. et al., 1996, A&A, 314, 87
Mastichiadis A., Kirk J. G., 1997, A&A, 320, 19
Press W. H. et al., 1989, Numerical Recipes in Fortran, Cambridge Univ. Press, Cambridge
Punch M. et al., 1992, Nat, 358, 477
Rybicki G., Lightman A. P., 1979, Radiative Processes in Astrophysics. Wiley Interscience, New York
Sreekumar P. et al., 1996, ApJ, 464, 628
Takahashi T. et al., 1996, ApJ, 470, L89
Ulrich M.-H., Maraschi L., & Urry C. M., 1997, ARA&A, 35, 445
Urry C. M. et al., 1997, ApJ, 486, 799
Zdziarski A. A., 1986, ApJ, 305, 45

This paper has been typeset from a TEX/LATEX file prepared by the author.